

Received May 8, 2014, accepted May 13, 2014, date of publication May 21, 2014, date of current version August 12, 2014.

Digital Object Identifier 10.1109/ACCESS.2014.2326165

SART-Type Half-Threshold Filtering Approach for CT Reconstruction

HENGYONG YU^{1,2}, (Senior Member, IEEE), AND GE WANG³, (Fellow, IEEE)

¹Department of Biomedical Engineering, Wake Forest University Health Sciences, Winston-Salem, NC 27157, USA

²Biomedical Imaging Division, VT-WFU School of Biomedical Engineering and Sciences, Winston-Salem, NC 27157, USA

³Biomedical Imaging Cluster, Department of Biomedical Engineering, Rensselaer Polytechnic Institute, Troy, NY 12180, USA

Corresponding author: H. Yu (hengyong-yu@ieee.org)

This work was supported in part by the National Institutes of Health/National Institute of Biomedical Imaging and Bioengineering under Grant EB011785, in part by the National Science Foundation (NSF) CAREER under Award CBET-1149679, and the NSF Collaborative Project under Grant DMS-1210967.

ABSTRACT The ℓ_1 regularization problem has been widely used to solve the sparsity constrained problems. To enhance the sparsity constraint for better imaging performance, a promising direction is to use the ℓ_p norm ($0 < p < 1$) and solve the ℓ_p minimization problem. Very recently, Xu *et al.* developed an analytic solution for the $\ell_{1/2}$ regularization via an iterative thresholding operation, which is also referred to as half-threshold filtering. In this paper, we design a simultaneous algebraic reconstruction technique (SART)-type half-threshold filtering framework to solve the computed tomography (CT) reconstruction problem. In the medical imaging field, the discrete gradient transform (DGT) is widely used to define the sparsity. However, the DGT is noninvertible and it cannot be applied to half-threshold filtering for CT reconstruction. To demonstrate the utility of the proposed SART-type half-threshold filtering framework, an emphasis of this paper is to construct a pseudoinverse transforms for DGT. The proposed algorithms are evaluated with numerical and physical phantom data sets. Our results show that the SART-type half-threshold filtering algorithms have great potential to improve the reconstructed image quality from few and noisy projections. They are complementary to the counterparts of the state-of-the-art soft-threshold filtering and hard-threshold filtering.

INDEX TERMS Compressive sampling, half-threshold filtering, discrete gradient transform, pseudo-inverse transform.

I. INTRODUCTION

Inspired by the theory of compressive sampling or compressive sensing (CS) [1], [2], the sparsity based computed tomography (CT) has been a hot topic for various applications such as dose reduction [3]–[5]. Because the x-ray attenuation coefficient often varies mildly within an anatomical component, and large changes are usually confined around borders of anatomical structures, the discrete gradient transform (DGT), a set of finite difference operators, has been widely utilized as a sparsifying operation in CS-inspired CT reconstruction such as in [3]–[5], whose ℓ_1 -norm is also referred to as the total variation (TV) [6], and the corresponding reconstruction techniques are called TV minimization. Recently, the soft-threshold nonlinear filtering [7] was proved to be a converging and efficient algorithm for the ℓ_1 -norm minimization regularized by a sparsity constraint. Unfortunately, because the DGT is non-invertible, the soft-threshold algorithm cannot be directly applied for TV minimization. To address this challenge, in 2010 we constructed soft-threshold filtering based pseudo-inverse

transforms for DGT and applied the soft-threshold filtering technique for image reconstruction from a limited number of projections [8].

It is well known that the sparsity is defined in terms of the ℓ_0 -norm in the CS theory [1], [2]. Due to the NP-hard problem, the ℓ_1 -norm is well accepted to replace the ℓ_0 -norm, making the optimization computationally manageable [1], [2]. However, the ℓ_1 -norm may yield inconsistent results and cannot recover a signal/image well in difficult cases such as highly limited measurements [9]. A promising direction is to use the ℓ_p -norm ($0 < p < 1$) to improve the sparsity of the reconstructed signal/image, which results in the so-called ℓ_p minimization problem [9], [10].

The ℓ_p regularization problem is a nonconvex, nonsmooth, and non-Lipschitz optimization problem. Generally speaking, it is nontrivial to have a thorough theoretical analysis and efficient algorithms. In the past years, the ℓ_p regularization problem was handled either by approximation [9] or reweighting techniques [11]. Based on a phase diagram study, Xu *et al.* showed that the ℓ_p regularization can generate

more sparse solutions than the ℓ_1 regularization and the $\ell_{\frac{1}{2}}$ regularization is, in a good sense, the most representative one among all ℓ_p [12]. When $p \in [\frac{1}{2}, 1)$, the smaller the value of p , the sparser solutions obtained by the ℓ_p regularization. When $p \in (0, \frac{1}{2}]$, the performance of ℓ_p regularization has no significant difference. More importantly, the solution of the $\ell_{\frac{1}{2}}$ regularization problem can be analytically expressed in a thresholding form, distinguishing it from others $\ell_p (0 < p < 1, p \neq \frac{2}{3})$ [13]. This finding results in a fast algorithm, similar to the iterative hard-threshold filtering algorithm for ℓ_0 regularization [14], [15] and the iterative soft-threshold filtering algorithm for ℓ_1 regularization [7].

In this paper we will apply the half-threshold filtering method to a simultaneous algebraic reconstruction technique (SART)-type CT image reconstruction framework to solve the $\ell_{\frac{1}{2}}$ regularization problem. Significant efforts will be made to construct a pseudo-inverse transform for DGT. The rest of this paper is organized as follows. In the next section, the mathematical principles of half-threshold filtering are summarized. In the third section, the SART-type framework for the $\ell_{\frac{1}{2}}$ regularization problem is designed in which a half-threshold filtering based pseudo-inverse transform is constructed for DGT. In the fourth section, preliminary numerical and experimental results are presented. Finally, the related issues are discussed in the last section.

II. HALF-THRESHOLD FILTERING APPROACH

Let $\mathbf{f} = [f_1, f_2, \dots, f_N]^T \in \mathbb{R}^N$ be an object function and $\mathbf{g} = [g_1, g_2, \dots, g_M]^T \in \mathbb{R}^M$ be a measured dataset. They are linked by the following linear system:

$$\mathbf{g} = \mathbf{A}\mathbf{f} + \mathbf{e}, \tag{1}$$

where $\mathbf{A} = (a_{m,n}) \in \mathbb{R}^M \times \mathbb{R}^N$ is the linear measurement matrix, and $\mathbf{e} \in \mathbb{R}^M$ the measurement noise. Let us define the ℓ_p norm of the vector \mathbf{f} as

$$\|\mathbf{f}\|_p = \left(\sum_{n=1}^N |f_n|^p \right)^{1/p}, \quad 0 < p < 1, \tag{2}$$

then, the ℓ_p regularization problem can be expressed as

$$\min_{\mathbf{f} \in \mathbb{R}^N} \left\{ \|\mathbf{g} - \mathbf{A}\mathbf{f}\|^2 + \lambda \|\mathbf{f}\|_p^p \right\}, \tag{3}$$

where $\lambda > 0$ is a free parameter to balance the two terms.

Now, let us construct a nonlinear function

$$h_{\lambda, \frac{1}{2}}(f_n) = \frac{2f_n}{3} \left(1 + \cos \left(\frac{2\pi}{3} - \frac{2}{3} \cos^{-1} \left(\frac{\lambda}{8} \left(\frac{|f_n|}{3} \right)^{-\frac{3}{2}} \right) \right) \right) \tag{4}$$

and a half-threshold operator

$$H_{\lambda, \frac{1}{2}}(f_n) = \begin{cases} h_{\lambda, \frac{1}{2}}(f_n) & |f_n| > \frac{3\sqrt[3]{2}}{4} \lambda^{2/3} \\ 0 & \text{otherwise.} \end{cases} \tag{5}$$

The corresponding half-thresholding algorithm for $\ell_{\frac{1}{2}}$ regularization (3) can be expressed as [13]

$$\mathbf{f}^{(k+1)} = \mathbf{H}_{\lambda^{(k)} \mu^{(k)}, \frac{1}{2}} \left(\mathbf{f}^{(k)} + \mu^{(k)} \mathbf{A}^T (\mathbf{g} - \mathbf{A}\mathbf{f}^{(k)}) \right), \tag{6}$$

where k indicates the iterative number instead of power for the variables, $\mu^{(k)}$ is a parameter for the updating of the intermediate image, and the operator $\mathbf{H}_{\lambda, \frac{1}{2}}(\mathbf{f}) = \left(H_{\lambda, \frac{1}{2}}(f_1), H_{\lambda, \frac{1}{2}}(f_2), \dots, H_{\lambda, \frac{1}{2}}(f_N) \right)^T$. For practical applications, we can choose $\mu^{(k)} = \mu^{(0)} = \frac{1}{\|\mathbf{A}\|^2}$, which means the normalization factor for the measurement matrix \mathbf{A} . The free parameter $\lambda^{(k)}$ can be chosen by cross-validation [13]. This half-threshold filtering is similar to the well known hard-threshold filtering

$$H_{\lambda, 0}(f_n) = \begin{cases} f_n & |f_n| > \sqrt{\lambda} \\ 0 & \text{otherwise} \end{cases} \tag{7}$$

for the ℓ_0 regularization [14] and the soft-threshold filtering

$$H_{\lambda, 1}(f_n) = \begin{cases} f_n - \text{sgn}(f_n) \frac{\lambda}{2} & |f_n| > \frac{\lambda}{2} \\ 0 & \text{otherwise} \end{cases} \tag{8}$$

for the ℓ_1 regularization [7]. Figure 1 shows several representative half-thresholding functions and the comparison for the half-threshold, hard-threshold and soft-threshold functions.

Because we have no specific assumptions on the system matrix \mathbf{A} in Eq. (6), this result can be directly applied to any linear system reconstruction problem including the CT reconstruction from a limited number of measurements under the framework of compressive sensing if there exists an invertible sparse transform of the imaging object. However, many practical sparse transforms are non-invertible, such as DGT. In the next section, we will develop a SART-type framework and construct a pseudo-inverse for DGT to enable the half-threshold filtering algorithm.

III. ALGORITHM DEVELOPMENT

A. IMAGING MODEL

For completeness, we will summarize the discrete imaging model [8], [16] as follows. In the context of CT reconstruction, a two-dimensional digital image can be expressed as $\mathbf{f} = (f_{i,j}) \in \mathbb{R}^I \times \mathbb{R}^J$, where the index $1 \leq i \leq I$ and $1 \leq j \leq J$ are integers. Define

$$f_n = f_{i,j}, \quad n = (i-1) \times J + j, \tag{9}$$

with $1 \leq n \leq N$ and $N = I \times J$, we can re-arrange the image into a vector for the measurement model Eq. (1). In this paper, both the signs $f_{i,j}$ and f_n are used for convenience. Each component of the function \mathbf{g} in Eq. (1) is a measured datum with M being the product of the number of projections and the number of detector elements. In a typical fan-beam geometry, the n^{th} pixel can be viewed as a rectangular region with a constant value f_n , the m^{th} measured datum g_m as an integral of the product between the x-ray linear attenuation coefficients and the corresponding weighted areas of pixels

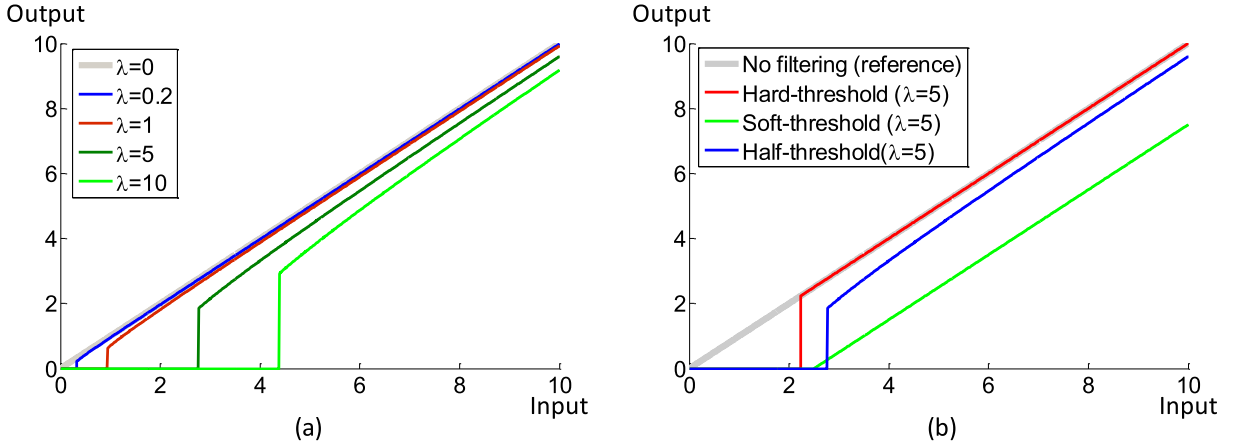


FIGURE 1. Half-threshold filtering. (a) Half-threshold filtering functions for different parameters; and (b) comparison of hard-threshold, soft-threshold and half-thresholding effects for the same parameter.

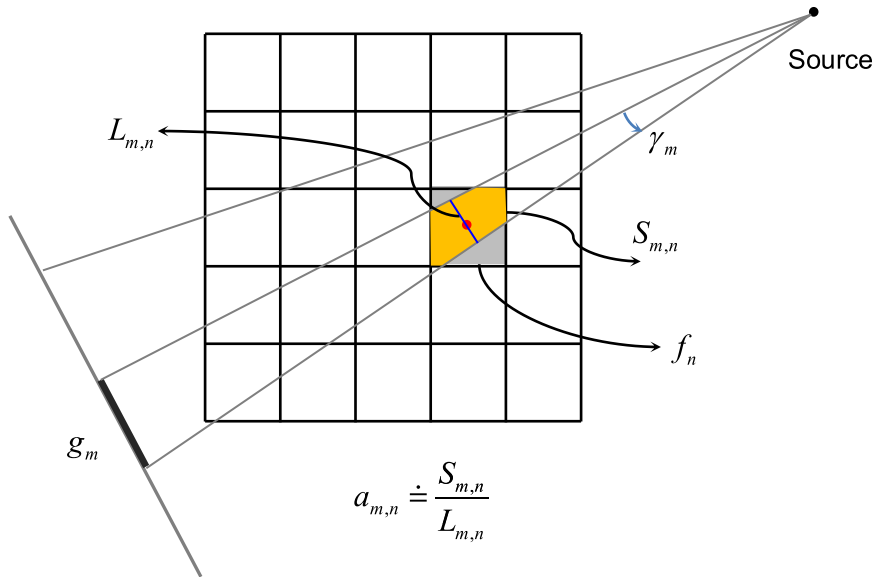


FIGURE 2. Discrete projection model assuming a discrete 2D image in fan-beam geometry.

partially covered by a narrow beam from an x-ray source to a detector element [16]. Thus, the component $a_{m,n}$ in Eq. (1) denotes the weighted interaction area between the n^{th} pixel and the m^{th} fan-beam path (Figure 2). While the whole matrix \mathbf{A} represents the forward projection, \mathbf{A}^T implements the back projection.

B. SART-TYPE RECONSTRUCTION FRAMEWORK

The SART-type solution for Eq. (1) can be written as [17]:

$$f_n^{(k+1)} = f_n^{(k)} + \mu^{(k)} \frac{1}{a_{+n}} \sum_{m=1}^M \frac{a_{m,n}}{a_{m+}} (g_m - \mathbf{A}_m \mathbf{f}^{(k)}), \quad (10)$$

where $a_{+n} = \sum_{m=1}^M a_{m,n} > 0$, $a_{m+} = \sum_{n=1}^N a_{m,n} > 0$, \mathbf{A}_m is the m^{th} row of \mathbf{A} , k is the iteration number, and $0 < \mu^{(k)} < 2$ is a free relaxation parameter. Let $\mathbf{\Lambda}^{+N} \in \mathbb{R}^N \times \mathbb{R}^N$ be a diagonal

matrix with $\Lambda_{n,n}^{+N} = \frac{1}{a_{+n}}$ and $\mathbf{\Lambda}^{M+} \in \mathbb{R}^M \times \mathbb{R}^M$ be a diagonal matrix with $\Lambda_{m,m}^{M+} = \frac{1}{a_{m+}}$, Eq. (10) can be rewritten as:

$$\mathbf{f}^{(k+1)} = \mathbf{f}^{(k)} + \mu^{(k)} (\mathbf{\Lambda}^{+N} \mathbf{A}^T \mathbf{\Lambda}^{M+} (\mathbf{g} - \mathbf{A} \mathbf{f}^{(k)})). \quad (11)$$

This implies that the solution Eq. (10) corresponds to the inner item “ $(\mathbf{f}^{(k)} + \mu^{(k)} \mathbf{A}^T (\mathbf{g} - \mathbf{A} \mathbf{f}^{(k)}))$ ” in Eq. (6) with $\mathbf{\Lambda}^{+N}$ and $\mathbf{\Lambda}^{M+}$ being weights for normalization of the matrix $\mathbf{A}^T \mathbf{\Lambda}$, which can be used for a better converging behavior.

When the imaging object \mathbf{f} is not sparse, to apply the half-threshold algorithm subject to a sparsity constraint, we must find a suitable sparse transform φ , under which the imaging object \mathbf{f} is sparse. Assume that \mathbf{f} can be sparsely represented as \mathbf{d} via φ , that is $\mathbf{d} = \varphi \mathbf{f}$. If φ is invertible, we have $\mathbf{f} = \varphi^{-1} \mathbf{d}$ where φ^{-1} is the inverse transform of φ . The half-threshold algorithm Eq. (6) can be modified as

$$\mathbf{f}^{(k+1)} = \varphi^{-1} \mathbf{H}_{\lambda^{(k)} \mu^{(k)}, \frac{1}{2}} \left(\varphi \left(\mathbf{f}^{(k)} + \mu^{(k)} \mathbf{A}^T (\mathbf{g} - \mathbf{A} \mathbf{f}^{(k)}) \right) \right), \quad (12)$$

and we have a SART-type half-threshold filtering framework for CT reconstruction

$$\mathbf{f}^{(k+1)} = \varphi^{-1} \mathbf{H}_{\lambda^{(k)}, \mu^{(k)}, \frac{1}{2}} \left(\varphi \left(\mathbf{f}^{(k)} + \mu^{(k)} \times \left(\mathbf{\Lambda}^{+N} \mathbf{A}^T \mathbf{\Lambda}^{M+} (\mathbf{g} - \mathbf{A} \mathbf{f}^{(k)}) \right) \right) \right). \quad (13)$$

Eq. (13) is the solution of the following $\ell_{\frac{1}{2}}$ regularization problem

$$\min_{\mathbf{f} \in \mathbb{R}^N} \left\{ \|\mathbf{g} - \mathbf{A} \mathbf{f}\|^2 + \lambda \|\varphi \mathbf{f}\|_{\frac{1}{2}} \right\}, \quad (14)$$

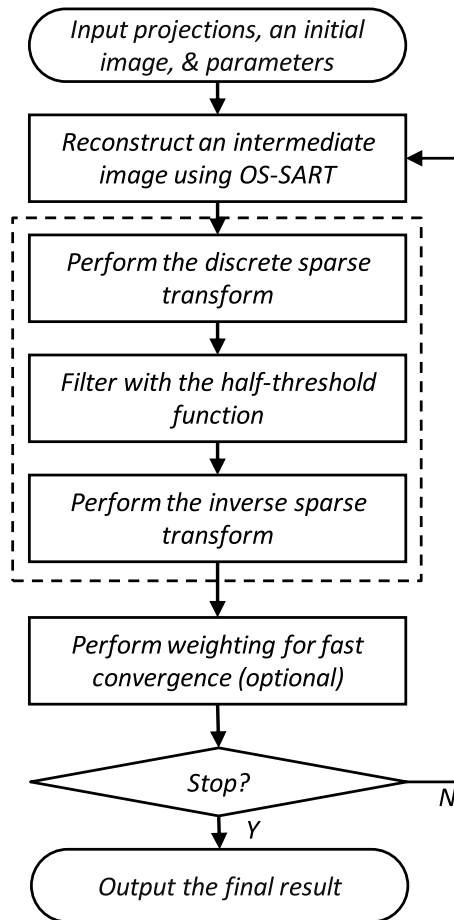


FIGURE 3. Algorithmic flowchart for half-thresholding based image reconstruction.

which is the corresponding modified version of Eq. (3) and has significant applications in the CT field. The flowchart of the SART-type half-thresholding framework Eq. (13) for the problem Eq. (14) is illustrated in Figure 3. It should be pointed out that Eq. (13) is a general formula depending on the definition of the filtering kernel \mathbf{H} . For example, if \mathbf{H} is defined as the soft-threshold or hard-threshold filtering kernel function, Eq. (13) can be viewed as the corresponding soft-threshold or hard-threshold filtering algorithms. As another example, the ℓ_p regularization problem also has analytic solutions when $p = \frac{2}{3}$, and Eq. (13) can be viewed as the corresponding algorithm if we define \mathbf{H} as the kernel function for $p = \frac{2}{3}$.

C. PSEUDO-INVERSE TRANSFORM OF THE DGT

In the medical imaging field, assuming a piecewise constant imaging model, the DGT has been widely used to define a sparsity constraint. Let us assume that a digital image satisfies the so-called Neumann conditions on the boundary:

$$\begin{aligned} f_{0,j} &= f_{1,j} \text{ and } f_{I,j} = f_{I+1,j} \text{ for } 1 \leq j \leq J, \\ f_{i,0} &= f_{i,1} \text{ and } f_{i,J} = f_{i,J+1} \text{ for } 1 \leq i \leq I. \end{aligned} \quad (15)$$

Then, the DGT in terms of standard isotropic discretization can be expressed as

$$d_{i,j} = \sqrt{(f_{i,j} - f_{i+1,j})^2 + (f_{i,j} - f_{i,j+1})^2}, \quad (16)$$

and the ℓ_p norm of the DGT can be expressed as

$$L_p(\mathbf{f}) = \left(\sum_{i=1}^I \sum_{j=1}^J |d_{i,j}|^p \right)^{\frac{1}{p}}. \quad (17)$$

When $p = 1$, Eq. (17) is the well known total variation. When $p = \frac{1}{2}$, the $\ell_{\frac{1}{2}}$ regularization problem in terms of DGT can be expressed as:

$$\min_{\mathbf{f} \in \mathbb{R}^N} \left\{ \|\mathbf{g} - \mathbf{A} \mathbf{f}\|^2 + \lambda \left(\sum_{i=1}^I \sum_{j=1}^J |d_{i,j}|^{\frac{1}{2}} \right) \right\}. \quad (18)$$

To apply the SART-type half-thresholding framework Eq. (13) to solve the problem Eq. (18), it requires to know the inverse transform of DGT. Unfortunately, the DGT is non-invertible. The solution Eq. (13) can not be directly applied to minimize Eq. (18). However, noticing the properties of iterative algorithms, we can construct a pseudo-inverse of the DGT based on the half-thresholding filtering. Assume that

$$\tilde{f}_n^{(k)} = f_n^{(k)} + \mu^{(k)} \frac{1}{a_{+n}} \sum_{m=1}^M \frac{a_{m,n}}{a_{m+}} (g_m - \mathbf{A}_m \mathbf{f}^{(k)}), \quad (19)$$

is the updated intermediate image from the projection constraint in the current iteration step k , which is exactly the same as Eq. (10). We can compute

$$d_{i,j}^{(k)} = \sqrt{(\tilde{f}_{i,j}^{(k)} - \tilde{f}_{i+1,j}^{(k)})^2 + (\tilde{f}_{i,j}^{(k)} - \tilde{f}_{i,j+1}^{(k)})^2}. \quad (20)$$

According to the half-threshold algorithm in Eqs. (5) & (6), when $d_{i,j}^{(k)} < w = \frac{3\sqrt{2}}{4} (\lambda^{(k)} \mu^{(k)})^{2/3}$ we can adjust the value of $\tilde{f}_{i,j}^{(k)}$, $\tilde{f}_{i+1,j}^{(k)}$ and $\tilde{f}_{i,j+1}^{(k)}$ to make $d_{i,j}^{(k)} = 0$, and when $d_{i,j}^{(k)} \geq w$ we can reduce the values of $(\tilde{f}_{i,j}^{(k)} - \tilde{f}_{i+1,j}^{(k)})^2$ and $(\tilde{f}_{i,j}^{(k)} - \tilde{f}_{i,j+1}^{(k)})^2$ to perform the half-thresholding filtering. That is, we can construct the following pseudo-inverse (see Appendix A for details of construction):

$$f_{i,j}^{(k+1)} = \frac{1}{4} (2f_{i,j}^{(k+1),a} + f_{i,j}^{(k+1),b} + f_{i,j}^{(k+1),c}), \quad (21)$$

$$f_{i,j}^{(k+1),a} = \begin{cases} \frac{2\tilde{f}_{i,j}^{(k)} + \tilde{f}_{i+1,j}^{(k)} + \tilde{f}_{i,j+1}^{(k)}}{4}, & \text{if } d_{i,j}^{(k)} < w \\ \frac{d_{i,j}^{(k)} + h_{\lambda^{(k)} \mu^{(k)}, \frac{1}{2}}(d_{i,j}^{(k)})}{2d_{i,j}^{(k)}} \tilde{f}_{i,j}^{(k)} + \frac{d_{i,j}^{(k)} - h_{\lambda^{(k)} \mu^{(k)}, \frac{1}{2}}(d_{i,j}^{(k)})}{4d_{i,j}^{(k)}} \\ \quad \times (\tilde{f}_{i+1,j}^{(k)} + \tilde{f}_{i,j+1}^{(k)}), & \text{if } d_{i,j}^{(k)} \geq w, \end{cases} \quad (22)$$

TABLE 1. Fixed values of λ for different algorithms in numerical simulations ($\eta = 50$).

Projection Number	21 (Noise-free)	21 (Noisy)	15 (Noise-free)	15 (Noisy)
$\ \mathbf{g} - \mathbf{A}\mathbf{f}\ ^2$	4.20×10^{-3}	2.39×10^{-2}	3.00×10^{-3}	1.69×10^{-2}
ℓ_1 -DGT	1.48×10^{-4}	8.43×10^{-4}	1.06×10^{-4}	5.95×10^{-4}
$\ell_{\frac{1}{2}}$ -DGT	1.30×10^{-4}	7.40×10^{-4}	0.93×10^{-4}	5.23×10^{-4}

$$f_{ij}^{(k+1),b} = \begin{cases} \frac{\tilde{f}_{ij}^{(k)} + \tilde{f}_{i-1,j}^{(k)}}{2}, & \text{if } d_{i-1,j}^{(k)} < w \\ \frac{d_{i-1,j}^{(k)} - h}{2d_{i-1,j}^{(k)}} \lambda^{(k)} \mu^{(k)} \tilde{f}_{i-1,j}^{(k)} + \frac{d_{i-1,j}^{(k)} + h}{2d_{i-1,j}^{(k)}} \lambda^{(k)} \mu^{(k)} \frac{1}{2} (d_{i-1,j}^{(k)}) \tilde{f}_{ij}^{(k)}, & \text{if } d_{i-1,j}^{(k)} \geq w, \end{cases} \quad (23)$$

$$f_{ij}^{(k+1),c} = \begin{cases} \frac{\tilde{f}_{ij}^{(k)} + \tilde{f}_{i,j-1}^{(k)}}{2}, & \text{if } d_{i,j-1}^{(k)} < w \\ \frac{d_{i,j-1}^{(k)} - h}{2d_{i,j-1}^{(k)}} \lambda^{(k)} \mu^{(k)} \tilde{f}_{i,j-1}^{(k)} + \frac{d_{i,j-1}^{(k)} + h}{2d_{i,j-1}^{(k)}} \lambda^{(k)} \mu^{(k)} \frac{1}{2} (d_{i,j-1}^{(k)}) \tilde{f}_{ij}^{(k)}, & \text{if } d_{i,j-1}^{(k)} \geq w. \end{cases} \quad (24)$$

Eq. (21) can be understood as a result of three consecutive steps in the dashed block in Figure 3. Because Eq. (21) serves as the inverse transform of DGT in the half-threshold filtering reconstruction framework, we call it a half-threshold filtering based pseudo-inverse of DGT.

IV. EXPERIMENTAL RESULTS

A. ANALYSIS OF THRESHOLD PARAMETER

Recall that the control parameter λ in Eq. (3) is to balance the data fidelity term $\|\mathbf{g} - \mathbf{A}\mathbf{f}\|^2$ and the penalty term $\|\mathbf{f}\|_p^p$. For different values of p , the value of $\|\mathbf{g} - \mathbf{A}\mathbf{f}\|^2$ is fixed and the values of $\|\mathbf{f}\|_p^p$ are different. To play similar roles for the penalty term, we should select different parameter λ for different p . However, for different value of p , the control parameter should satisfy $\lambda(p) \|\mathbf{f}\|_p^p = C$, where C is a constant. For practical applications, the constant C can be estimated as $C = \eta \|\mathbf{g} - \mathbf{A}\mathbf{f}\|^2$ which is the data fidelity term multiplying by a scale factor η . Meanwhile, $\|\mathbf{f}\|_p^p$ can also be estimated. As a results, we can estimate $\lambda(p)$ as

$$\lambda(p) = \frac{\eta \|\mathbf{g} - \mathbf{A}\mathbf{f}\|^2}{\|\mathbf{f}\|_p^p}. \quad (25)$$

When a sparsifying transform ϕ is considered, $\|\mathbf{f}\|_p^p$ in Eq. (25) can be replaced by $\|\phi\mathbf{f}\|_p^p$. Therefore, a uniform scale factor η can provide a fair comparison for the performance of different p in terms of ℓ_p norm regularization.

B. NUMERICAL SIMULATION

To verify the correctness and demonstrate the advantages of the proposed SART-type half-threshold filtering algorithms, we implemented them in MatLab and performed numerical tests. We assumed a representative circular scanning locus of radius 57.0 cm and fan-beam geometry. The object was a modified Shepp-Logan phantom in a compact support with a radius of 10.0 cm. We used an equidistant virtual detector array of length 20.0 cm. The detector was centered at the system origin and made perpendicular to the direction from the origin to the x-ray source. The detector array consisted of 300 elements. For each of our selected numbers of projections over a full-scan range, we first equiangularly acquired the corresponding projection dataset based on the discrete projection model shown in Fig. 2. Then, we reconstructed the images using the following two methods for DGT: the ℓ_1 -norm minimization with soft-threshold filtering proposed in [8], and the $\ell_{\frac{1}{2}}$ norm minimization with half-threshold filtering proposed in this paper. Furthermore, the fast weighting method [18] was used to accelerate the convergence of all the SART-type iterative reconstruction algorithms.

For all the above methods, the parameter $\mu^{(k)}$ in the SART iteration formula in Eq. (13) was set to be a constant 1.0, and the stopping criterion was defined as reaching a maximum iteration number. For noise-free projections, the data fidelity term should be zero under the ideal condition which is impractical. In our applications, $\|\mathbf{g} - \mathbf{A}\mathbf{f}\|^2$ was set to 3.0×10^{-3} and 4.2×10^{-3} for 15 and 21 views, respectively. A fixed scale factor $\eta = 50$ was used for a fair comparison and the estimated values of the threshold λ for different algorithms were listed in Table 1. Figure 4 shows the converging curves for the root of mean square error (RMSE) with the fixed scale factor 50, where the RMSE is computed for the reconstructed intermediate image in refer to the ground truth phantom image. Figure 5 shows the corresponding reconstructed 256×256 images after stop of the iterations. For practical applications, measurement noise is unavoidable. To test the stability of the proposed algorithms against data noise, we repeated the aforementioned reconstructions from projections corrupted by Poisson noise, assuming 5×10^4 photons per detector element [19]. The estimated values of threshold λ were listed in Table 1, and the results were also shown in Figures 4 and 5, which confirm the stability of the proposed algorithms.

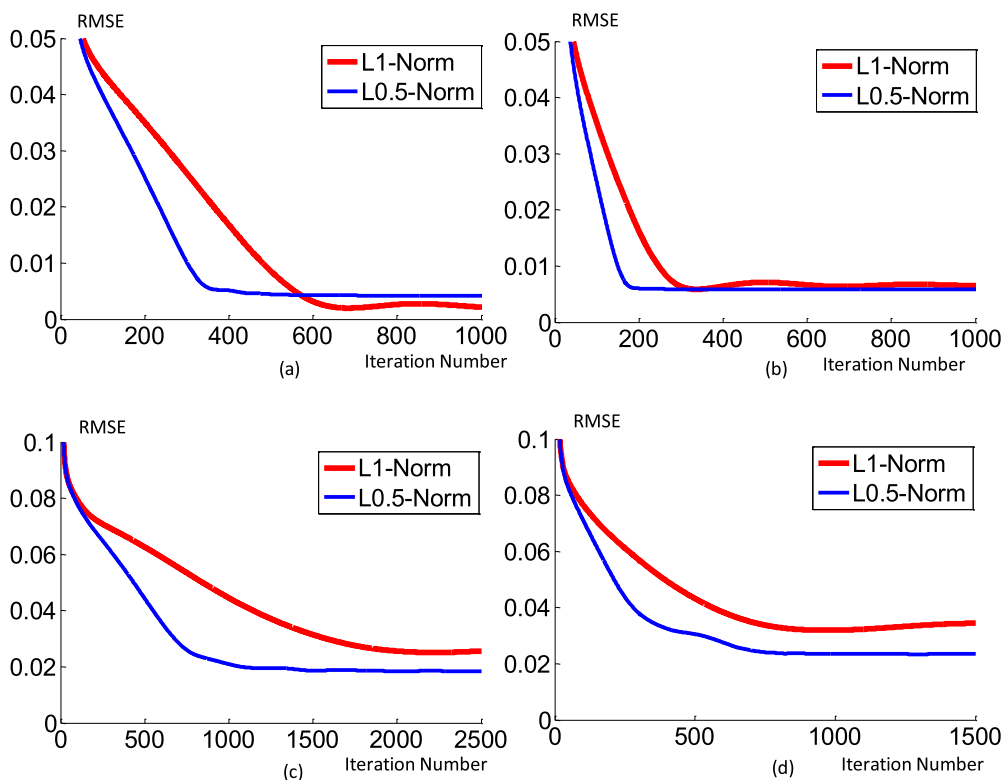


FIGURE 4. Converging curves of RMSE with a fixed scale factor $\eta = 50$ for the representative algorithms with digital gradient transform. While the plots for (a) were reconstructed from 21 noise-free projections, the plots for (c) were from 15 noise-free projections. (b) and (d) are the counterparts of (a) and (c) from noisy projections.

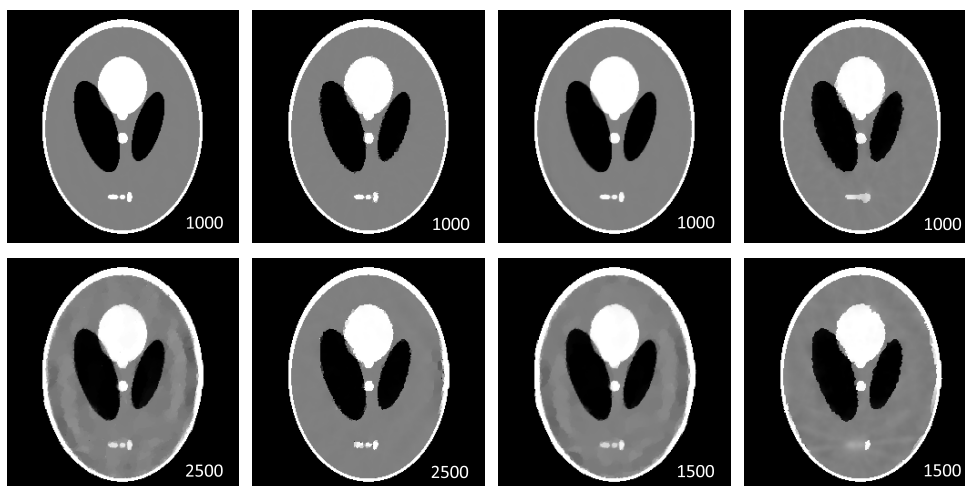


FIGURE 5. Reconstructed images of a refined Shepp-Logan phantom using a fixed scale factor $\eta = 50$. From left to right, the first and second columns are the reconstructions from noise-free projections using soft-threshold and half-threshold filtering, respectively, and the third and fourth columns are the counterparts of the first and second columns reconstructed from noisy projections. While the first row images are from 21 projections, the second row images are from 15 projections. The white number in each image indicates the maximum iteration number. The display window is $[0.1, 0.3]$.

C. SELECTION OF OPTIMAL THRESHOLD PARAMETER

If the sparsity knowledge of the imaging object is known, that is, the non-zero component number of the sparse transform of the imaging object, we can dynamically select the optimal parameter $\lambda^{(k)}$ for fast convergence during the iteration.

Assuming that there are Q non-zero components among the component values in the transform domain, we can descend those values and pickup the $Q+1$ component d_{Q+1} , and the optimal $\lambda^{(k)}$ can be determined as $\lambda^{(k)} = \frac{4\sqrt{6}}{9} (d_{Q+1})^{\frac{3}{2}}$ [13]. For example, for the aforementioned 256×256 Shepp-Logan

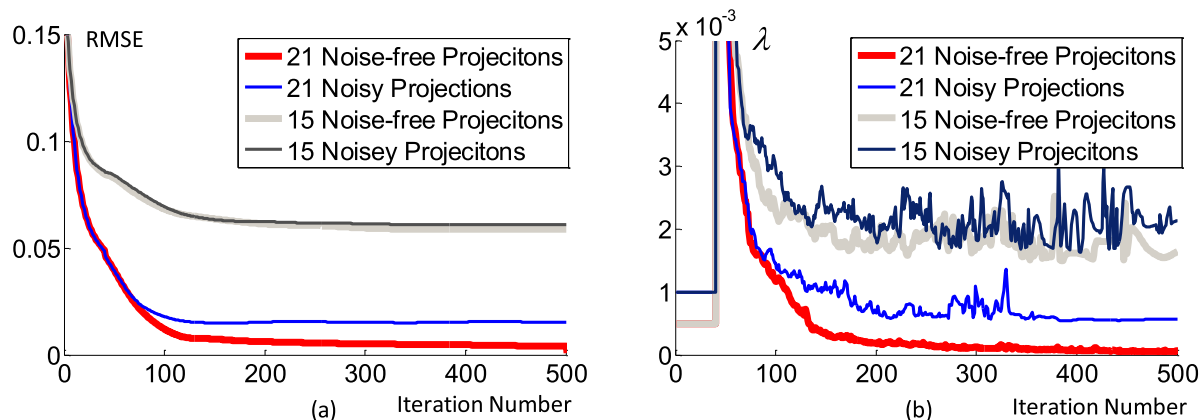


FIGURE 6. Converging curves for the images reconstructed using the prior information of the sparsity. While (a) shows the converging curves of RMSE, (b) shows the curves of the corresponding optimal threshold values.

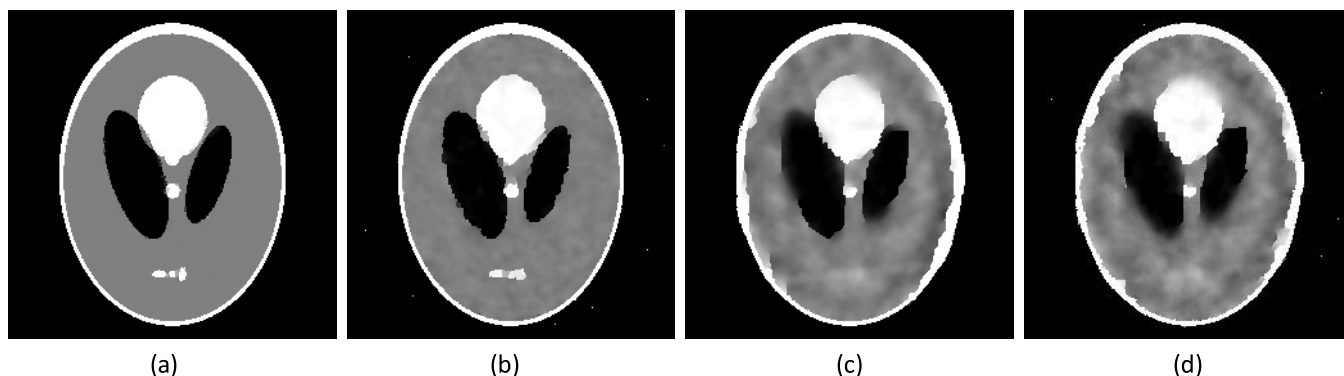


FIGURE 7. Reconstructed images of a refined Shepp-Logan phantom after 500 iterations using the prior information of sparsity in a display window [0.1 0.3]. (a) is the image reconstructed from 21 noise-free projections, and (c) is reconstructed from 15 noise-free projections. (b) and (d) are the counterparts of (a) and (c) from noisy projections.

TABLE 2. RMSEs of the reconstructed images after the stop of iterations.

Projection Number	21 (Noise-free)	21 (Noisy)	15 (Noise-free)	15 (Noisy)
Fixed λ ($\eta = 50$)	0.0042 (1000)	0.0059 (1000)	0.0185 (2500)	0.0235 (1500)
Optimized λ	0.0040 (500)	0.0154 (500)	0.0589 (500)	0.0611 (500)

phantom, there are 2194 non-zero components in the corresponding DGT image, and we can compute the optimal threshold based on the 2195th maximum value of the DGT. To verify this point, we repeated the above experiments and used a prior knowledge of $Q = 2500$. Because in the first several iterations the images are smooth due to the data consistency has not been fully enhanced, we adopted a fixed threshold for the first 40 iterations and the prior knowledge of $Q = 2500$ was employed after that. The iteration number 40 was selected empirically and the heuristic rule is to obtain a rough image before stopping the fixed threshold method. Figure 6 shows the converging curves for RMSE and the optimal threshold parameter $\lambda^{(k)}$. The detailed reconstructed images and their RMSEs after the stop of the iterations are in Figure 7 and Table 2. From Figures 4-7 and Table 2, we can see that the dynamically selected optimal thresholds can result in the fastest convergence speed. However,

they do not guarantee the best image quality. Obviously, with the increasement of the iterative number and using the developed half-threshold filtering based ℓ_1 -norm minimization method with the dynamically selecting of the optimal parameter, the reconstructed image quality becomes better and better, and eventually the reconstructed image will converge to the original image phantom if there is no noise and the projections are sufficient for exact reconstruction guided by the CS theory. This point can be further demonstrated by Figure 8, where a narrower display window [0.19, 0.21] is used to magnify the artifacts to demonstrate the high accuracy.

D. PHANTOM EXPERIMENT

A phantom experiment was performed on a GE Discovery CT750 HD scanner at Wake Forest University Health

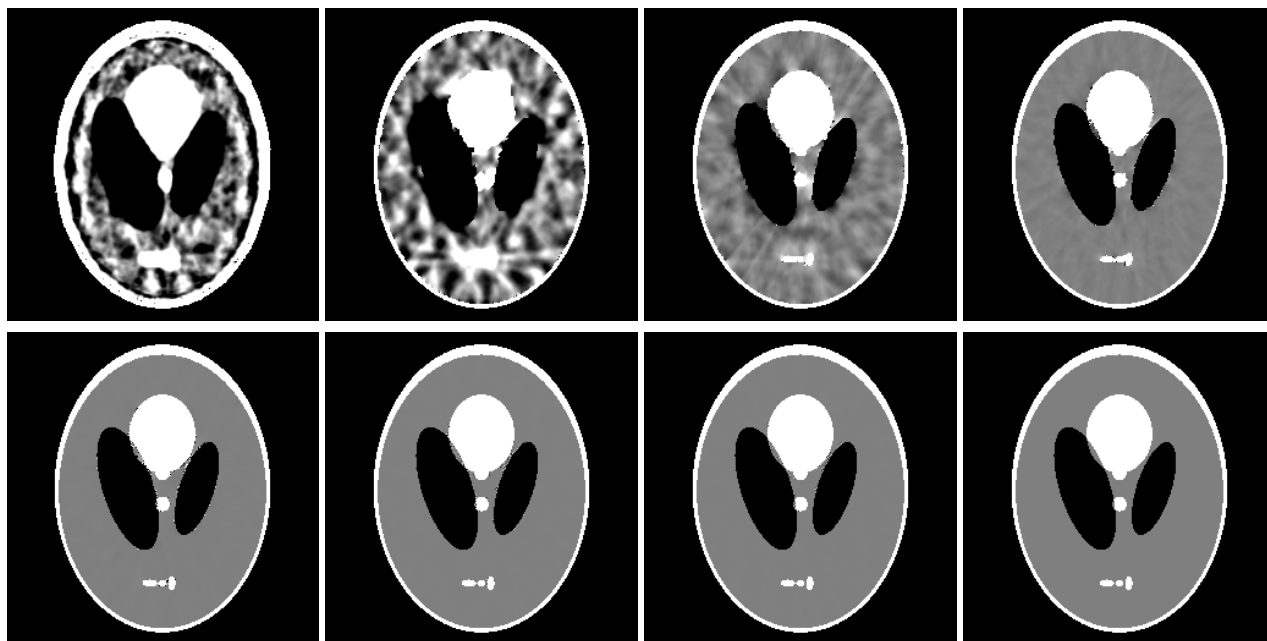


FIGURE 8. Reconstructed images of the refined Shepp-Logan phantom from 21 noise-free projections after different numbers of iterations using DGT and the prior information of sparsity. From top to bottom and from left to right, the numbers of iterations for the first 7 images are 50, 100, 200, 500, 1000, 1500 and 2000 respectively. The last image is the ideal phantom. The display window is [0.19, 0.21].

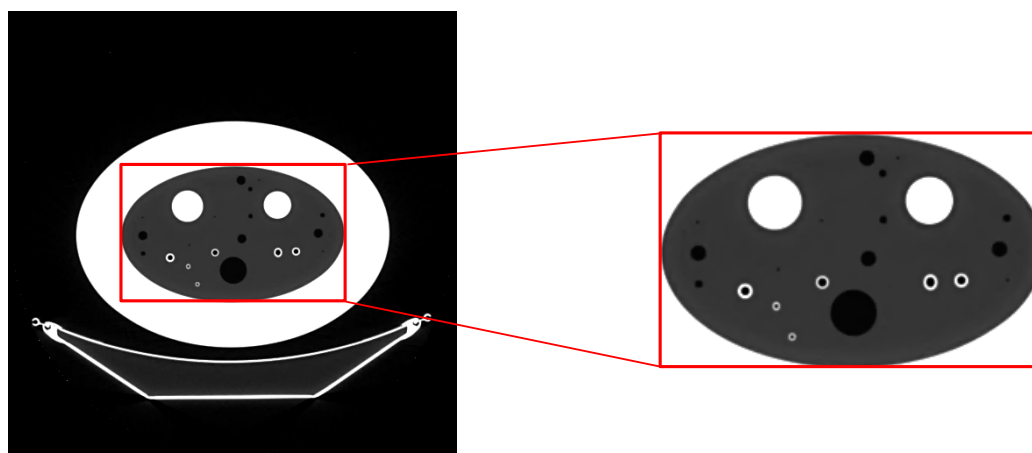


FIGURE 9. Reference image for the phantom experiment reconstructed from 984 projections using the OS-SART method in a display window [−1000HU, −200HU].

TABLE 3. Fixed values of λ for different algorithms in numerical simulations.

Projection Number	17	27	49
ℓ_1 -DGT	1.5949	1.4207	1.2240
$\ell_{\frac{1}{2}}$ -DGT	2.7061	2.4106	2.0769

Sciences with a circular scanning trajectory. After appropriate pre-processing, we obtained a sinogram of the central slice in typical equi-angular fan-beam geometry. The radius of the scanning trajectory was 538.5 mm. Over a 360° range, 984

projections were uniformly acquired. For each projection, 888 detector elements were equi-angularly distributed, which defines a FOV of a 249.2 mm radius and an iso-center spatial resolution of 584 μm . Because the true image is

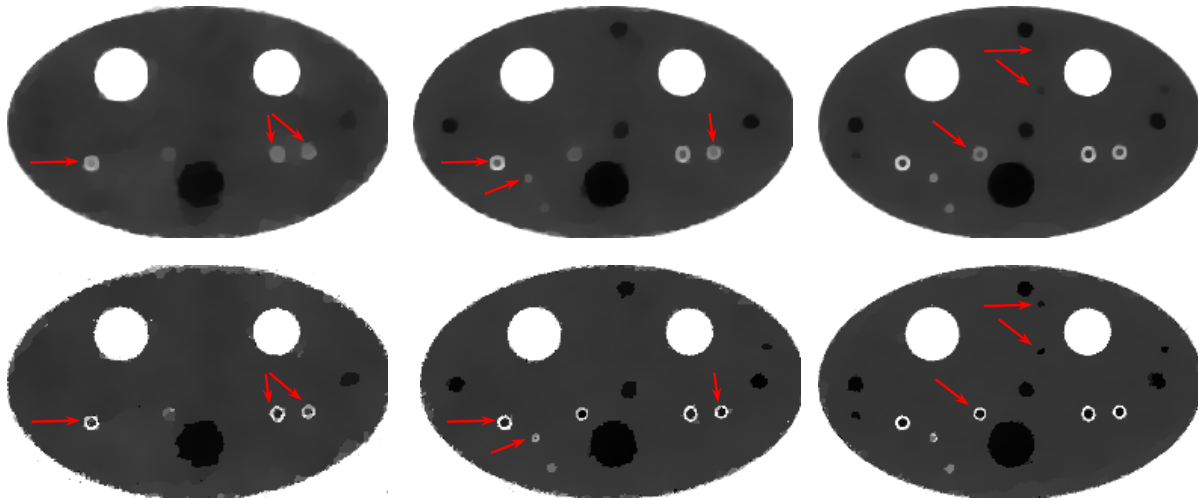


FIGURE 10. Magnified parts of the reconstructed physical phantom images from few-view projections in a display window $[-1000\text{HU}, -200\text{HU}]$. From left to the right, the view numbers are 17, 27 and 49, respectively. While the top row images were reconstructed by the soft-threshold algorithm, the bottom row images were reconstructed by the proposed half-threshold filtering algorithm. The red arrows indicate the difference between the soft-threshold and half-threshold filtering based reconstructions.

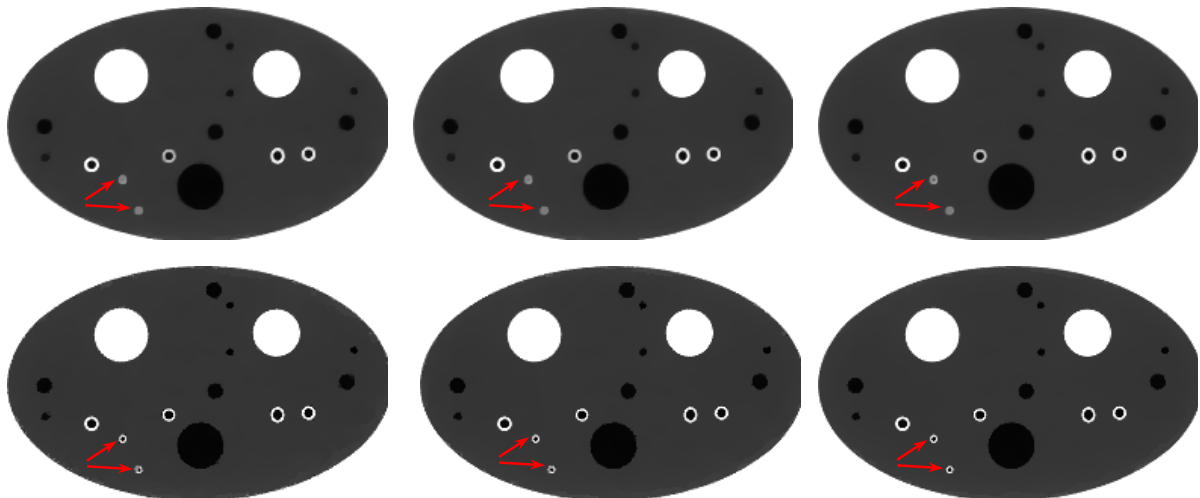


FIGURE 11. Magnified parts of the reconstructed physical phantom images from sufficient projections in a display window $[-1000\text{HU}, -200\text{HU}]$. From left to the right, the view numbers are 164, 246 and 492, respectively. While the top row images were reconstructed by the soft-threshold algorithm, the bottom row images were reconstructed by the proposed half-threshold filtering algorithm. The red arrows indicate the difference between the soft-threshold and half-threshold filtering based reconstructions.

not available, a reference image was reconstructed by the OS-SART method from full projections of 984 views with the subset number being 8 and the iteration number being 20 (see Figure 9). To simulate a scan of sparse projections, we uniformly undersampled projections by discarding 19/35/56 in every 20/36/57 views to obtain 49/27/17 views. For a fixed scale factor and view number, the estimated values of the threshold λ for different algorithms were listed in Table 3. Because the $\ell_{1/2}$ regularization problem is a nonconvex function and the iteration may converge to a local minimum, a good initial guess may lead to a better solution. Therefore, the reconstruction results of the soft-threshold filtering approach after 200 iterations were employed as the initial guesses, and the final results after 300 iterations (500 iterations in total) were shown in Figure 10. In reference to the image

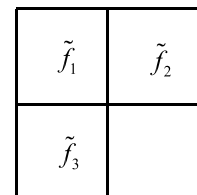


FIGURE 12. Locations of the pixels used in Eq. (A.1).

reconstructed from full views in Figure 9, the results in Figure 10 confirm that the developed half-threshold filtering based $\ell_{1/2}$ -norm minimization outperforms the soft-threshold filtering based ℓ_1 -norm minimization for few-view reconstruction problems.

V. DISCUSSIONS AND CONCLUSION

This is a follow-up paper of our previous work on the soft-threshold filtering based ℓ_1 -norm minimization for CT reconstruction [8]. Both the papers share the same algorithmic structure but differ significantly in norm definitions and filtering schemes. Because DGT is not invertible, it cannot be directly applied to the half-threshold filtering based algorithms. Similar to what we did in [8], we have constructed half-threshold filtering based pseudo-inverse transforms of DGT. Different from the truly invertible transforms, these pseudo-inverses take advantage of the reconstructed images from the previous iterations. It is pointed out that the construction method for pseudo-inverse transforms is nonunique, and the readers can construct other possible transforms in the spirit of the above-described strategy and in reference to additional prior knowledge. In addition to the DGT in terms of standard isotropic discretization, there are other possible sparse transforms. For example, we can define a discrete difference transform (DDT) [8]

$$d_{i,j} = |f_{i,j} - f_{i+1,j}| + |f_{i,j} - f_{i,j+1}|. \quad (26)$$

Similar to what we have done in [8], we can construct a half-threshold filtering based pseudo-inverse of DDT. It is easy to verify that the pseudo-inverse of DDT shares the same formulas Eqs. (21-24) to DGT except the computation of $d_{i,j}^{(k)}$.

From Figures 4-7, it can be seen that the half-threshold filtering based algorithms outperform the soft-threshold filtering based counterpart when the projections are rather few and noisy (e.g., 15 noisy projections). When the projection number is not too few (e.g. 21 noise-free projections), while the half-threshold filtering based algorithms converge fast, the soft-threshold filtering based algorithms eventually produce slightly better results, and all the results can be viewed as accurate (see the first row images of Figure 5). This point can be further demonstrated by the physical phantom reconstruction results from sufficient number of projections (see Figure 11). This phenomenon may be due to the following two reasons. First, the projections are sufficient for accurate image reconstruction for both of the soft-threshold and half-threshold filtering methods. Second, while the half-threshold filtering method converges to a local minimal point, the soft-threshold filtering method converges to the global minimum point. Because the constructed pseudo-inverse of the DGT is undercomplete, the developed synthesis-type half-threshold algorithm for $\ell_{\frac{1}{2}}$ -norm minimization should be equivalent and complementary to the corresponding analysis approaches [20]. Regarding the computational complexity, our analysis shows that computational cost of the half-threshold filtering step for the sparsity constrain is less than 1% of the that of the OS-SART updating step for the data fidelity constraint. Therefore, the total computational cost of the proposed half-threshold filtering method is almost the same as that of the original OS-SART method.

Clearly, the constructed pseudo-inverse transforms can also be regarded as non-linear filters. However, we prefer calling them pseudo-inverse transforms, because they serve as inverse transforms of DGT after the half-threshold filtration defined by Eq. (6) in the framework of half-threshold filtering framework. While Xu *et al* pointed out that the solutions of the general ℓ_p ($0 < p < 1, p \neq \frac{2}{3}, p \neq \frac{1}{2}$) regularization cannot be analytically expressed in a thresholding form [13], it is our hypothesis that we can approximate those solutions using appropriate threshold functions. For a given ℓ_p regularization problem, we can first numerically find the relationship between the inputs and outputs, then fit the parameters of a threshold function, and finally construct a pseudo-inverse if the sparse transform is non-invertible. A possible approximation can be expressed as

$$H_{\lambda,p}(f_n) = \begin{cases} f_n + \text{sgn}(f_n)\omega_2(\lambda, p)|f_n|^{\omega_3(\lambda,p)} & |f_n| > \omega_1(\lambda, p) \\ 0 & \text{otherwise,} \end{cases} \quad (27)$$

where $\omega_1(\lambda, \rho)$, $\omega_2(\lambda, \rho)$ and $\omega_3(\lambda, \rho)$ are three parameter functions to be numerically fitted.

In conclusion, we have applied the half-threshold filtering principle for CT image reconstruction subject to a sparsity constraint, constructed a pseudo-inverse transform for DGT, and demonstrated the faster convergence and better image quality in well-defined practical scenarios. It is encouraging that the numerical and phantom experimental results have shown that the half-threshold filtering based algorithm outperforms the soft-threshold filtering based algorithm in the cases of few view noisy data. This is in consistent with the common sense that the ℓ_p -norm ($p < 1$) regularization can reconstruct sparser solutions than the ℓ_1 -norm regularization. Therefore, it is complementary to the counterparts of the state-of-the-art soft-threshold filtering and hard-threshold filtering. We are motivated to proceed along this direction for practical applications. Because the ℓ_p regularization problem is a nonconvex, nonsmooth, and non-Lipschitz optimization problem, strategies will be investigated to escape from local minima to the global minimum in the near future.

APPENDIX A: PSEUDO-INVERSE TRANSFORM OF DGT BASED ON THE HALF-THRESHOLDING FILTERING

To simplify the notation, let us denote $w = \frac{3\sqrt[3]{2}}{4} (\lambda^{(k)} \mu^{(k)})^{2/3}$. As shown in Fig. 12 we only consider the discrete gradient

$$d = \sqrt{(\tilde{f}_1 - \tilde{f}_2)^2 + (\tilde{f}_1 - \tilde{f}_3)^2}. \quad (\text{A.1})$$

Case I: $d < w$

When $d < w$, the half-threshold filtering requires to adjust the values of \tilde{f}_1 , \tilde{f}_2 and \tilde{f}_3 to make $d = 0$. Because Eq. (A.1) implies that $\tilde{f}_1 - \tilde{f}_2 = 0$ when $d = 0$, we can assign the new value $f_1 = f_2 = \frac{\tilde{f}_1 + \tilde{f}_2}{2}$ to satisfy $\tilde{f}_1 - \tilde{f}_2 = 0$. Similarly, we can assign the new value $f_1 = f_3 = \frac{\tilde{f}_1 + \tilde{f}_3}{2}$ to satisfy $\tilde{f}_1 - \tilde{f}_3 = 0$.

However, $f_1 = \frac{\tilde{f}_1 + \tilde{f}_2}{2}$ and $f_1 = \frac{\tilde{f}_1 + \tilde{f}_3}{2}$ are inconsistent. Hence, we can use their average as the final adjustment. That is, we have

$$\begin{cases} f_1 = \frac{2\tilde{f}_1 + \tilde{f}_2 + \tilde{f}_3}{4} \\ f_2 = \frac{\tilde{f}_1 + \tilde{f}_2}{2} \\ f_3 = \frac{\tilde{f}_1 + \tilde{f}_3}{2}. \end{cases} \quad (\text{A.2})$$

Case II: $d \geq w$

When $d \geq w$, the half-threshold filtering requires to adjust the values of \tilde{f}_1 , \tilde{f}_2 and \tilde{f}_3 for d to become $h_{\lambda^{(k)}\mu^{(k)}, \frac{1}{2}}(d)$. For this purpose, we use a multiplicative factor $\beta = \frac{h_{\lambda^{(k)}\mu^{(k)}, \frac{1}{2}}(d)}{d}$ and obtain

$$h_{\lambda^{(k)}\mu^{(k)}, \frac{1}{2}}(d) = \sqrt{(\tilde{f}_1 - \tilde{f}_2)^2 \beta^2 + (\tilde{f}_1 - \tilde{f}_3)^2 \beta^2}. \quad (\text{A.3})$$

This implies that we can set $|f_1 - f_2| = \beta|\tilde{f}_1 - \tilde{f}_2|$ and $|f_1 - f_3| = \beta|\tilde{f}_1 - \tilde{f}_3|$. To satisfy $|f_1 - f_2| = \beta|\tilde{f}_1 - \tilde{f}_2|$, one possible way is to assign

$$\begin{cases} f_1 = \tilde{f}_1 - \frac{(1-\beta)(\tilde{f}_1 - \tilde{f}_2)}{2} = \frac{d+h_{\lambda^{(k)}\mu^{(k)}, \frac{1}{2}}(d)}{2d}\tilde{f}_1 \\ \quad + \frac{d-h_{\lambda^{(k)}\mu^{(k)}, \frac{1}{2}}(d)}{2d}\tilde{f}_2 \\ f_2 = \tilde{f}_2 - \frac{(1-\beta)(\tilde{f}_2 - \tilde{f}_1)}{2} = \frac{d-h_{\lambda^{(k)}\mu^{(k)}, \frac{1}{2}}(d)}{2d}\tilde{f}_1 \\ \quad + \frac{d+h_{\lambda^{(k)}\mu^{(k)}, \frac{1}{2}}(d)}{2d}\tilde{f}_2. \end{cases} \quad (\text{A.4})$$

Similarly, we can assign

$$\begin{cases} f_1 = \tilde{f}_1 - \frac{(1-\beta)(\tilde{f}_1 - \tilde{f}_3)}{2} = \frac{d+h_{\lambda^{(k)}\mu^{(k)}, \frac{1}{2}}(d)}{2d}\tilde{f}_1 \\ \quad + \frac{d-h_{\lambda^{(k)}\mu^{(k)}, \frac{1}{2}}(d)}{2d}\tilde{f}_3 \\ f_3 = \tilde{f}_3 - \frac{(1-\beta)(\tilde{f}_3 - \tilde{f}_1)}{2} = \frac{d-h_{\lambda^{(k)}\mu^{(k)}, \frac{1}{2}}(d)}{2d}\tilde{f}_1 \\ \quad + \frac{d+h_{\lambda^{(k)}\mu^{(k)}, \frac{1}{2}}(d)}{2d}\tilde{f}_3 \end{cases} \quad (\text{A.5})$$

to satisfy $|f_1 - f_3| = \beta|\tilde{f}_1 - \tilde{f}_3|$. Again, due to the inconsistency between values of f_1 in (A.4) and (A.5), we take their average and obtain

$$\begin{cases} f_1 = \frac{d+h_{\lambda^{(k)}\mu^{(k)}, \frac{1}{2}}(d)}{2d}\tilde{f}_1 + \frac{d-h_{\lambda^{(k)}\mu^{(k)}, \frac{1}{2}}(d)}{4d}(\tilde{f}_2 + \tilde{f}_3) \\ f_2 = \frac{d-h_{\lambda^{(k)}\mu^{(k)}, \frac{1}{2}}(d)}{2d}\tilde{f}_1 + \frac{d+h_{\lambda^{(k)}\mu^{(k)}, \frac{1}{2}}(d)}{2d}\tilde{f}_2 \\ f_3 = \frac{d-h_{\lambda^{(k)}\mu^{(k)}, \frac{1}{2}}(d)}{2d}\tilde{f}_1 + \frac{d+h_{\lambda^{(k)}\mu^{(k)}, \frac{1}{2}}(d)}{2d}\tilde{f}_3. \end{cases} \quad (\text{A.6})$$

We can obtain the weighted mean Eq. (21) from Eqs. (A.2) and (A.6).

ACKNOWLEDGMENT

This work was partially supported by the NIH/NIBIB Grant EB011785, the NSF CAREER Award CBET-1149679, and the NSF Collaborative project DMS-1210967.

REFERENCES

- [1] D. L. Donoho, "Compressed sensing," *IEEE Trans. Inf. Theory*, vol. 52, no. 4, pp. 1289–1306, Apr. 2006.
- [2] E. J. Candes, J. Romberg, and T. Tao, "Robust uncertainty principles: Exact signal reconstruction from highly incomplete frequency information," *IEEE Trans. Inf. Theory*, vol. 52, no. 2, pp. 489–509, Feb. 2006.
- [3] J. Yang, H. Yu, M. Jiang, and G. Wang, "High-order total variation minimization for interior SPECT," *Inverse Problems*, vol. 28, no. 1, pp. 015001–1–015001-24, 2012.
- [4] H. Yu and G. Wang, "Compressed sensing based interior tomography," *Phys. Med. Biol.*, vol. 54, no. 9, pp. 2791–2805, 2009.
- [5] G. H. Chen *et al.*, "Prior image constrained compressed sensing (PICCS) and applications in X-ray computed tomography," *Current Med. Imag. Rev.*, vol. 6, no. 2, pp. 119–134, 2010.
- [6] L. I. Rudin, S. Osher, and E. Fatemi, "Nonlinear total variation based noise removal algorithms," *Phys. D*, vol. 60, nos. 1–4, pp. 259–268, 1992.
- [7] I. Daubechies, M. Defrise, and C. De Mol, "An iterative thresholding algorithm for linear inverse problems with a sparsity constraint," *Commun. Pure Appl. Math.*, vol. 57, no. 11, pp. 1413–1457, 2004.
- [8] H. Yu and G. Wang, "A soft-threshold filtering approach for reconstruction from a limited number of projections," *Phys. Med. Biol.*, vol. 55, no. 13, pp. 3905–3916, 2010.
- [9] R. Chartrand and V. Staneva, "Restricted isometry properties and non-convex compressive sensing," *Inverse Problems*, vol. 24, no. 3, p. 14, 2008.
- [10] R. Chartrand, "Exact reconstruction of sparse signals via nonconvex minimization," *IEEE Signal Process. Lett.*, vol. 14, no. 10, pp. 707–710, Oct. 2007.
- [11] I. F. Gorodnitsky and B. D. Rao, "Sparse signal reconstruction from limited data using FOCUSS: A re-weighted minimum norm algorithm," *IEEE Trans. Signal Process.*, vol. 45, no. 3, pp. 600–616, Mar. 1997.
- [12] Z.-B. Xu, H.-L. Guo, Y. Wang, and H. Zhang, "Representative of $L_{1/2}$ regularization among L_q ($0 < q \leq 1$) regularizations: An experimental study based on phase diagram," *Acta Autom. Sinica*, vol. 38, no. 7, pp. 1225–1228, 2012.
- [13] Z. Xu, X. Chang, F. Xu, and H. Zhang, " $L_{1/2}$ regularization: A thresholding representation theory and a fast solver," *IEEE Trans. Neural Netw. Learn. Syst.*, vol. 23, no. 7, pp. 1013–1027, Jul. 2012.
- [14] T. Blumensath and M. E. Davies, "Iterative thresholding for sparse approximations," *J. Fourier Anal. Appl.*, vol. 14, nos. 5–6, pp. 629–654, 2008.
- [15] T. Blumensath and M. E. Davies, "Iterative hard thresholding for compressed sensing," *Appl. Comput. Harmonic Anal.*, vol. 27, no. 3, pp. 265–274, 2009.
- [16] H. Y. Yu and G. Wang, "Finite detector based projection model for high spatial resolution," *J. X-Ray Sci. Technol.*, vol. 20, no. 2, pp. 229–238, 2012.
- [17] G. Wang and M. Jiang, "Ordered-subset simultaneous algebraic reconstruction techniques (OS-SART)," *J. X-Ray Sci. Technol.*, vol. 12, no. 3, pp. 169–177, 2004.
- [18] A. Beck and M. Teboulle, "A fast iterative shrinkage-thresholding algorithm for linear inverse problems," *SIAM J. Imag. Sci.*, vol. 2, no. 1, pp. 183–202, 2009.
- [19] H. Yu, Y. Ye, S. Zhao, and G. Wang, "Local ROI reconstruction via generalized FBP and BPF algorithms along more flexible curves," *Int. J. Biomed. Imag.*, vol. 2006, Article ID: 14989, 2006.
- [20] M. Elad, P. Milanfar, and R. Rubinstein, "Analysis versus synthesis in signal priors," *Inverse Problems*, vol. 23, no. 3, pp. 947–968, 2007.



HENGYONG YU (SM'06) is an Assistant Professor and the Director of the CT Laboratory, Department of Biomedical Engineering, Wake Forest University Health Sciences, Winston-Salem, NC, USA. He received the bachelor's degrees in information science and technology, and computational mathematics, and the Ph.D. degree in information and communication engineering from Xi'an Jiaotong University, Xi'an, China, in 1998, 1998, and 2003, respectively. He was an Instructor and Associate Professor with the College of Communication Engineering, Hangzhou Dianzi University, Hangzhou, China, from 2003 to 2004. From 2004 to 2006, he was a Post-Doctoral Fellow and an Associate Research Scientist with the Department of Radiology, University of Iowa, Iowa City, IA, USA. From 2006 to 2010, he was a Research Scientist and the Associate Director of the CT Laboratory with the Biomedical Imaging Division, VT-WFU School of Biomedical Engineering and Sciences, Virginia Tech, Blacksburg, VA, USA. He joined Wake Forest University Health Sciences as a Faculty Member in 2010. His current interests include computed tomography and medical image processing. He has authored and co-authored more than 100 peer-reviewed journal papers with an H-index of 19 according to the web of knowledge. He is the Founding Editor-in-Chief of *JSM Biomedical Imaging Data Papers*, serves as an Editorial Board Member for *Signal Processing*, *Journal of Medical Engineering*, *CT Theory and Applications*, *International Journal of Biomedical Engineering and Consumer Health Informatics*, and *Open Medical Imaging Journal*, and the Guest Editor of the IEEE TRANSACTIONS ON MEDICAL IMAGING, the IEEE ACCESS, and *International Journal of Biomedical Imaging*. He is a Senior Member of the IEEE Engineering in Medicine and Biology Society, and a member of American Association of Physicists in Medicine and the Biomedical Engineering Society. In 2005, he was honored for an outstanding doctoral dissertation by Xi'an Jiaotong University, and was a recipient of the first prize for best natural science paper from the Association of Science and Technology of Zhejiang Province. He was also a recipient of an NSF CAREER Award for the development of CS-based interior tomography in 2012.



GE WANG (F'03) received the Ph.D. degree in electrical and computer engineering. He is a Clark and Crossan Endowed Chair Professor and the Director of the Biomedical Imaging Center/Cluster, Rensselaer Polytechnic Institute, Troy, NY, USA. His expertise includes X-ray computed tomography (CT), optical molecular tomography, omni-tomography, and informetrics. He wrote the first paper on spiral/helical multislice/cone-beam CT, which is currently a main mode of CT scanners with 100-million multislice/cone-beam scans annually performed worldwide. He is the lead author of the first paper on bioluminescence tomography, and holds initial patents. His group published the first papers and holds patents on interior tomography and omni-tomography for grand fusion of all relevant tomographic modalities (*all-in-one*) to acquire different datasets simultaneously (*all-at-once*) and capture multiphysics interactions (*all-of-couplings*) with CT-MRI and CT-SPECT as examples. His results were featured in *Nature*, *Science*, and PNAS, and recognized with various academic awards. He has authored more than 375 journal papers, in addition to numerous conference articles, presentations, and patents. His group has been in long-term collaboration with the General Electric Global Research Center, Wake Forest Institute Regenerative Medicine, ZEISS/Xradia, and others, and continuously funded by federal agents (\$25 M as PI/Contact PI/Multi-PI, \$28 M as Co-PI/Co-I/Mentor). He is the Lead Guest Editor of four IEEE TRANSACTIONS ON MEDICAL IMAGING special issues on X-ray CT, molecular imaging, compressive sensing, and spectral CT, respectively, the Founding Editor-in-Chief of *International Journal of Biomedical Imaging*, an Associate Editor of the IEEE TRANSACTIONS ON MEDICAL IMAGING and the MEDICAL PHYSICS JOURNAL. He is a fellow of SPIE, OSA, AIMBE, and AAPM, and welcomes research and educational opportunities.

• • •